

# A novel interfacial induced nucleation and accurate self-seeding via membrane assisted cooling crystallization

Wu Xiao<sup>1</sup>, Zeman He<sup>2</sup>, Peiyu Li<sup>2</sup>, Xuehua Ruan<sup>3</sup>, Xiaoming Yan<sup>3</sup>, Xiangcun Li<sup>4</sup>, and Gaohong He<sup>4</sup>

<sup>1</sup>Dalian Univeristy of Technology

<sup>2</sup>School of Chemical Engineering

<sup>3</sup>Dalian Univeristy of Technology at Panjin

<sup>4</sup>Dalian University of Technology

May 5, 2020

## Abstract

Accurate cooling crystallization is vitally important in the production of highly specialized fine chemicals and pharmaceutical engineering, etc. Herein, a novel hollow fiber membrane-assisted cooling crystallization (MACC) was developed to achieve precise nucleation and self-seeding process control. Poly-tetrafluoroethylene (PTFE) and polyethersulfone (PES) membrane with diverse interfacial induced nucleation and thermal conduction properties were introduced to accelerate the nucleation and then transfer the automatically detached crystal seed into the crystallizer. Polymeric membrane can dominate the nucleation kinetic and hinder the secondary nucleation, which was validated from the theoretical model and on-line detective experiments. The crystal product manufactured by MACC possessed better morphology, larger mean size ( $>1.35$  mm), higher purity ( $>99.5$  wt%) and narrower size distribution than the conventional cooling crystallization. Space-time process decoupling between nucleation and crystal growth can be realized via auto-screening uniform nuclei in the membrane modules and controllable growth in the crystallizer during MACC.

## Introduction

Crystallization is an extremely important separation unit operation, which is used in the production of highly specialized fine solid products<sup>1-3</sup>. Cooling crystallization, one of classic crystallization process, is mostly controlled by adding seed crystals within the metastable zone to induce nucleation<sup>4-7</sup>. Successful artificial seeding operation depends on a lot of aspects, seed size and amount, time point and place of addition, and experience of the operator, etc. However, conventional cooling crystallization that requires external seed adding procedure are suffered the risk of the secondary nucleation, which will limit the crystal purity, morphology and particle size distribution<sup>11,12</sup>, etc.

Recently, researchers are working to select and add seed by using molecular sieves or additional physical fields (electric, magnetic, etc.)<sup>8-11</sup>. However, none of these methods can achieve the automate seeding with accurate temperature control. In addition, nucleation induced via seeding crystals and crystal growth kinetics in the crystallizer determine the essential solid product quality and fundamentally influence further downstream processing (solid-liquid separation, drying, etc.). Decoupling the competition between nucleation and crystal growth from space and time aspect simultaneously is the core concern for all the researcher.

As a highly designable and environmentally friendly material, membrane obtains a great development in many fields related to crystallization process<sup>12-15</sup>. One of the most impressive applications is the membrane served as a heterogeneous nucleation interface to trigger the nucleation process<sup>16,17</sup>. When the membrane unit concentrating the solution via selectively mass transfer of the solvent, the supersaturated solution on

the membrane surface become nucleation and the formed particles can auto-detach from the surface under proper dynamic force field<sup>18,19</sup>. This finding is of importance for the accurate control of the mass transfer related crystallization process (evaporative crystallization, antisolvent crystallization, e.g.).

Inspiring transfer features of hollow fiber membrane also shed light on the heat exchange and the relevant process control<sup>20</sup>. In addition, with the high packing density, hollow fiber membrane module ensures the high manufacture capacity for potential industrial applications<sup>21-23</sup>. The total heat transfer coefficient of the hollow fiber membrane module can be as high as 2000 W/(m<sup>2</sup>·K); the ratio between the heat transfer coefficient of hollow fiber membrane heat exchangers verse the volume was 2 to 15 times higher than that of commercial metal heat exchangers, showing impressive application advantages<sup>24-26</sup>. Moreover, the potential advantage of hollow fiber membrane module on the accurate heat exchange and temperature distribution is an interesting topic. All the above properties of the hollow fiber membrane can potentially benefit the cooling crystallization control via heterogenous nucleation and high heat transfer efficiency, which had not fully unfolded and in-depth investigated.

Thiourea, a fundamental chemicals in many industrial fields<sup>27-31</sup>, was commonly manufactured via cooling crystallization. Nowadays, high-purity thiourea plays more and more irreplaceable role as the electrocatalytic materials and battery materials<sup>32,33</sup>, which raised the urgent requirement on accurate nucleation and growth control of its cooling crystallization process<sup>34,35</sup>.

In this work, we proposed a new cooling crystallization control mechanism to prepare high-purity thiourea crystals via introducing the polymeric hollow fiber membrane module. The membrane module is functioning as the key devices for inducing the nucleation and self-seeding. Poly-tetrafluoroethylene (PTFE) and poly-ethersulfone (PES) hollow fiber membrane were investigated on their thermal conductivities and inducing nucleation properties. In this membrane-assisted cooling crystallization (MACC), the surface induced nucleation and accurate self-seeding will be validated from theoretical and experimental aspects. The feasible accurate and automatic control MACC process was then compared with the conventional cooling crystallization (with seeding and none seeding) in terms of thiourea crystal purity, morphology and crystal size distribution (CSD) to fully reveal its advantages in nucleation and crystal growth control.

## 2. Theory of MACC

A schematic diagram of the ideal MACC process is shown in Figure 1. The crystallization solution and the cooling liquid flow along the shell side and tube side of the membrane module, respectively. When the coolant feed into the hollow fiber membrane module, it can decrease the temperature of the crystallization solution to the metastable zone effectively due to the outstanding heat exchange property of the membrane module. The operation pressure difference and temperature difference on the two sides of the membrane are both small, thus, there is only heat transfer on the membrane surface, and the transmembrane mass transfer can be ignored. The induced nucleus on the supercooling membrane surface then migrates from the membrane surface to the bulk crystallization solution under the proper flow conditions. To describe this complicated dynamic process, the relevant model should be introduced.

### 2.1 Nucleation induction period with membrane interfacial involved.

The nucleation induction period  $t_{\text{ind}}$  is defined as the time interval from the solution reaches the supersaturated state to the solid particles appear and is detected.  $t_{\text{ind}}$  is commonly introduced and measured as a critical crystallization parameter to evaluate the crystallization operation, which can be affected by factors such as supersaturation, stirring strength and external interfacial, physical field, etc.<sup>13,36,37</sup>The presence of external crystal seeds usually shorten the induction period.

It is generally believed that the induction period is inversely proportional to the primary nucleation rate  $B_p$  of the crystal, namely<sup>38,39</sup>,

$$t_{\text{ind}} \propto B_p^{-1} \quad (1)$$

The initial nucleation rate equation expressed by the Arrhenius reaction rate can be written as:

$$B_p = A \exp\left[-\frac{16\pi\gamma^3 V_m^2}{3\kappa^3 T^3 (\ln s)^2}\right] \quad (2)$$

Where  $A$  is an exponential factor;  $V_m$  is a molar volume;  $\kappa$  is Boltzmann constant, and  $\gamma$  is the surface tension of the crystallization solution. Thus, the induction period  $t_{\text{ind}}$  can be expressed as,

$$\frac{16\pi\gamma^3 V_m^2 + K}{3\kappa^3 T^3 (\ln s)^2} \quad (3)$$

where  $K$  is a system dependent constant.

Therefore, under constant temperature conditions,  $\ln t_{\text{ind}}$  and  $(\ln s)^{-2}$  follows the linearly relationship, and the slope of the line is defined as  $\alpha$ ,

$$\alpha = \frac{16\pi\gamma^3 V_m^2}{3\kappa^3 T^3} \quad (4)$$

The surface tension of heterogeneous nucleation is directly impacted by the hydrophilic characteristics between the membrane surface and the crystallization system. As the case of complete non-affinity between the crystalline solid and the foreign solid surface (corresponding to the complete non-wetting in liquid-solid systems), the contact angle  $\theta = 180^\circ$ . The overall free energy of nucleation is the same as that required for homogeneous nucleation. For the case of partial affinity (the partial wetting of a solid with a liquid),  $0 < \theta < 180^\circ$ , which indicates that nucleation is easier to achieve because the overall excess free energy required is less than that for homogeneous one. For the case of complete affinity (complete wetting),  $\theta = 0$ , and the free energy of nucleation is equal to zero. Therefore, the solid-liquid surface tension  $\gamma$  in the presence of the introduced membrane interface can be obtained from the above formula.

$$\gamma = \left[ f \frac{3\alpha\kappa^3 T^3}{16\pi V_m^2} \right]^{\frac{1}{3}} \quad (5)$$

where  $f$  is coefficient related to the contact angle, and expressed as followed,

$$f = \frac{(2 + \cos\theta)(1 - \cos\theta)^2}{4}$$

equation (6)

In principle, the induction period will decrease with the declining surface tension. Thus, solid-liquid surface tension  $\gamma$  is an important thermodynamic parameter for the nucleation and growth process of crystal, especially for the novel crystallization process involved heterogenous interface (MACC, e.g.), which will be discussed in the later section.

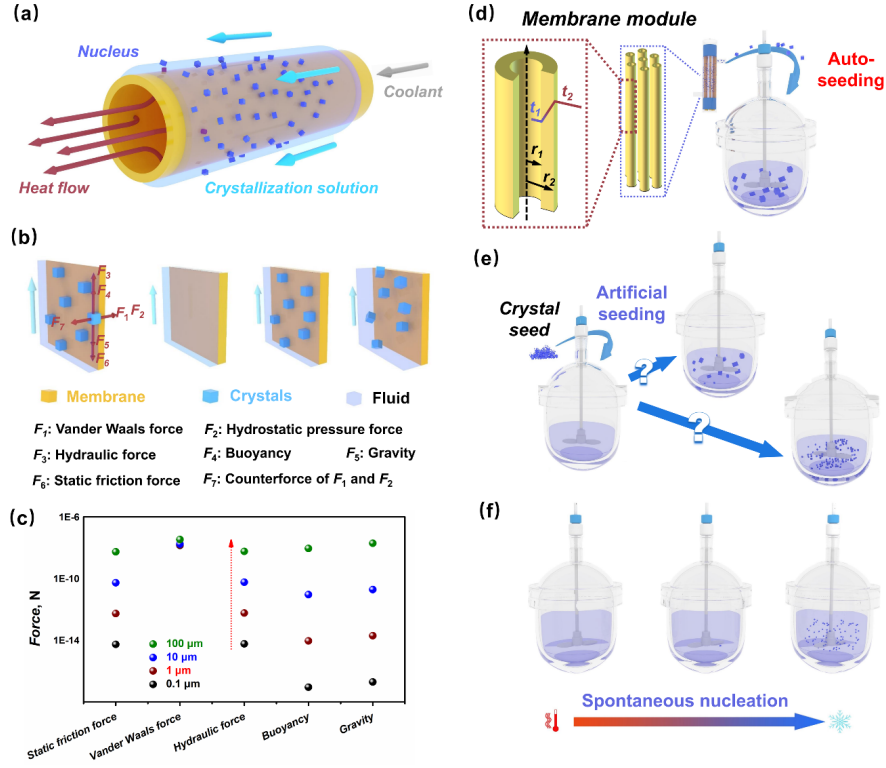


**Figure 1.** Principle of MACC and comparison with classic cooling crystallizations. (a) Schematic diagram of the ideal MACC process; (b) Micro force field model of surface induced nucleation and self-seeding process (c) Comparison of the different force acting on the crystal with different size; (d) Heat transfer model of membrane module in MACC; (e) cooling crystallization with artificial seeding; (f) cooling crystallization with spontaneous nucleation.

## 2.2 Membrane based self-seeding process.

In the membrane assisted crystallization, beyond the heterogeneous interface to accelerate heterogeneous nucleation, the hollow fiber membrane possesses the additional function. The crystals appeared on the membrane surface will then fall off with the flow of the fluid, entering the crystallizer. The micro force field model on the crystal particle-membrane surface to analyze this process is illustrated as followed.

As defined Figure 1b,  $F_1$ ,  $F_2$  and  $F_3$  represent the intermolecular forces (mainly van der Waals forces), hydrostatic pressure force and hydraulic forces, respectively;  $F_5$  and  $F_6$  are gravity and static friction;  $F_7$  is the reaction force of  $F_1$  and  $F_2$ .  $F_1 \sim F_5$  can be expressed by the following formula<sup>40-43</sup>,

$$F_1 = \frac{A}{6} \left( \frac{rr_c}{Z_0^2(r_c+r)} + \frac{r_c}{(Z_0+r)^2} \right) \quad (7)$$

$$F_2 = 1.7 \times 6\pi\mu r_c v_{r_c} \quad (8)$$

$$v_{r_c} = \frac{3r_c}{h} U_m \quad (9)$$

$$F_3 = \rho_l g H L^2 \quad (10)$$

$$F_4 = \rho_l g L^3 \quad (11)$$

$$F_5 = \rho_c g L^3 \quad (12)$$

Where  $L$  and  $r_c$  are the crystal size and the spherical equivalent radius of the crystal, respectively.  $A$  is the Hamaker constant (the general order is  $10^{-20}\text{J}$ ).  $r$  is the roughness of the membrane surface;  $Z_0$  is the

distance between the crystal and the membrane surface;  $\rho_f$  and  $\rho_c$  are the density of the fluid and the crystal, respectively;  $g$  is the acceleration of gravity and  $H$  is the position of the crystal in the fluid;  $\mu$  is the fluid viscosity;  $v_{r_c}$  represents the velocity of the fluid at the center of the crystal;  $h$  represents the thickness of the fluid layer;  $U_m$  is the average velocity of the fluid.

According to the principle of force balance, the forces in the horizontal and vertical directions of the crystal have the following relationship<sup>43</sup>,

$$F_7 = F_1 + F_2 \quad (13)$$

$$F_6 = F_3 + F_4 - F_5 \quad (14)$$

In MACC, when the crystal is inclined to detach from the surface of the separation membrane, the overall force acting on the crystal at the membrane surface must satisfy the following formulas<sup>43</sup>,

$$F_3 + F_4 - F_5 \geq F_{\max} \quad (15)$$

$$F_{\max} = K(F_1 + F_2) \quad (16)$$

Where  $F_{\max}$  the maximum static friction force of certain crystal, and  $K$  is the maximum static friction coefficient. Based on the equation, the criterion for the crystal to slide or detach from the membrane surface can be expressed as<sup>43</sup>,

$$\frac{1.7 \times 6\pi\mu r_c \frac{3r_c}{h} U_m + (\rho_f - \rho_c)gL^3}{\rho_f gHL^2 + \frac{A}{6} \left( \frac{r r_c}{Z_0^2 (r_c + r)} + \frac{r_c}{(Z_0 + r)^2} \right)} \geq K \quad (17)$$

The relationship of the different force acting on the crystal with different size was shown in Figure 1c. As discussed in authors' previous work, the value of the crystal detach criterion can be increased first and then decreased to zero as the crystal size increases<sup>19</sup>. This means that the tiny seeds detached from the surface of the separation membrane have a relatively concentrated particle size distribution due to the auto-selection mechanism based on the micro force field of the membrane surface (also illustrated in Figure 1b). Only the crystals within a certain interval can detach from the membrane surface. According to Eq. (7) to (12), the peak of the crystal detachment curve or the detachment space varies with the fluid flow rate, viscosity and roughness of the separation membrane. Thus, the overall MACC process is shown in Figure 1d. The nucleus first produces crystals on the membrane, then grows to a certain extent and detaches from the membrane surface into the membrane module (achieving the 'auto-seeding' process). Thereafter, the crystal is transported to the crystallizer to complete the following growth process. According to Figure 1c, the detachment motion and the auto-seeding process are highly size-dependent. Thus, different from the artificial seeding operation (Figure 1e), the seeding operation in MACC became automatically and controllable. These crystal particles as seeds are uniformly transported through the membrane module to the crystallizer and continue to grow in the low supersaturation of the bulk solution. By provided abundant nucleus with uniform initial size, MACC can avoid the explosive nucleation and exceeding secondary nucleation that easily occurred in conventional cooling crystallization (especially the spontaneous nucleation operation, shown in Figure 1f).

### 2.3 Heat transfer model in the membrane module.

As a cooling process, the heat transfer process determines the membrane surface temperature, which also determines the nucleation driving force. As shown in Figure 1d, the ideal hollow fiber membrane can be regarded as a cylindrical wall. The inner and outer radius of the cylindrical wall are respectively  $r_1$  and  $r_2$ ; the membrane length is  $L$ ; the temperatures of the inner and outer surfaces are maintained at constant temperatures  $t_1$  and  $t_2$ , respectively.

As a simplified model, for the membrane length exceeds more than ten times of the outer diameter of the membrane outer diameter, both ends of the heat transfer area of the cylindrical wall is negligible, and the axial direction and the circumferential direction thermal conductivity is also negligible. The temperature varies only on the radial direction, named one-dimensional steady-state heat conduction of the long cylindrical wall. Unlike flat wall heat transfer, the heat transfer area of the cylinder wall is not constant and varies

with radius. When solving the radial heat conduction problem of the cylindrical wall, it is convenient to apply the cylindrical coordinate system. A one-dimensional steady-state heat transfer equation describing the absence of an internal heat source is<sup>44,45</sup>,

$$\frac{d}{dr} \left( r \frac{dt}{dr} \right) = 0 \quad (18)$$

The boundary conditions are shown as followed<sup>45</sup>,

$$r = r_1, t = t_1; r = r_2, t = t_2 \quad (19)$$

The solution satisfying the above boundary conditions is<sup>45</sup>,

$$t = t_1 - \frac{t_1 - t_2}{\ln\left(\frac{r_2}{r_1}\right)} \ln \frac{r}{r_1} \quad (20)$$

The above equation shows that the temperature distribution is the logarithm of  $r$  when radial heat conduction through the cylinder wall function. With the decreasing  $r$ , the temperature gradient can also be modified with a high accuracy on the one-dimensional, which is a nonnegligible features of heat transfer process via a hollow fiber membrane module.

According to Fourier's law, the heat transfer rate through the wall of the radius  $r$  is,

$$\Phi = -\lambda A \frac{dt}{dr} \quad (21)$$

where  $A$  represents the surface area of the cylinder wall,  $A = 2\pi rL$ .  $\frac{dt}{dr}$  represents temperature gradient.

A single-layer cylindrical wall steady-state heat transfer rate equation can be obtained,

$$\Phi = \frac{2\pi L(r_2 - r_1)\lambda(t_1 - t_2)}{(r_2 - r_1) \ln \frac{r_2}{r_1}} = \frac{(A_2 - A_1)\lambda(t_1 - t_2)}{(r_2 - r_1) \ln \frac{A_2}{A_1}} = \lambda A_m \frac{t_1 - t_2}{b} = \frac{\Delta\tau}{R}$$

englishR(22)

where  $b$  represents thickness of the cylinder wall, m.  $R$  represents thermal resistance of the cylindrical wall,  $R = \frac{b}{\lambda A_m}$ , °C/w.  $A_m$  represents Logarithmic average area,  $m^2$ . The hollow fiber membrane is compared to a hollow cylinder having a thickness. The thermal conductivity and the thickness of the cylinder are jointly considered to illustrate the heat transfer in the hollow fiber membrane module. With the model above and known thermal conductivity of the membrane materials, we can predict the interfacial supercooling degree and then carry out further nucleation and growth kinetic simulation.

### 3. Experiments

#### 3.1 Materials and membrane module.

Thiourea was provided by Shandong Jingbo Yifeng Co., Ltd, and the purity was around 98%). Ultrapure water was produced by a laboratorial water purification system (Liaoning Rightleder Environmental Engineering Co., China, LTLD-P50, the conductivity lower than  $0.05 \mu\text{s cm}^{-1}$ ). PTFE hollow fiber membrane was produced in Dongda Water Industry Group Co., Ltd. and the PES hollow fiber membrane was produced in the authors' laboratory.

#### 3.2 Characterization of membrane.

The surface and cross section morphology of membranes were observed using a field-emission scanning electron microscope (FE-SEM, NOVA NanoSEM 450, FEI, USA). The surface roughness was measured with an atomic force microscope (AFM; Dimension ICON, Bruker, USA). The porosity of the membranes was determined by means of the software called Image Pro Plus. Solution contact angle (CA) of membrane was evaluated using the JC2000D machine (POWEREACH<sup>®</sup>, Shanghai zhongchen, China). The thermal conductivity of the PTFE and the PES hollow fiber membrane at different temperatures was measured using a thermal conductivity meter (TC3200, XIATECH, China). Since the hydrophilicities of the two membranes were different, the porosity of PTFE and PES hollow fiber membrane were measured by density measurement and water absorption measurement, respectively.

The microstructure of the two membranes are shown in Figure 2. PTFE hollow fiber membrane is a microporous membrane with very small surface porosity, which can be considered as a symmetric membrane with uniform cross section structure. PES hollow fiber membrane does not have apparent pore with nano scale on the surface and the cross section of the membrane indicates its asymmetric structure with a thin skin layer. The characteristics of the membrane and homemade membrane module are listed in Table 1 and Table 2, respectively. Membrane modules with different packaging density  $\varphi$  were assembled to evaluate their nucleation inducing performance.

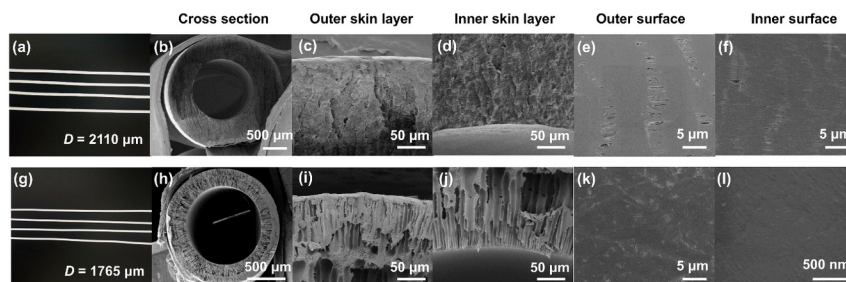


**Figure 2.** SEM for the microstructure of PTFE membrane (a-f) and PES membrane (g-l).

**Table 1.** Key parameters of PTFE and PES hollow fiber membrane.

Material	Outer Diameter ( $\mu\text{m}$ )	Inner Diameter ( $\mu\text{m}$ )	Water Contact Angle ( $^\circ$ )	Volumetric Porosity	thermal conductivity* (W/m-K)	Mean Roughness (nm)
PTFE	2110 $\pm$ 50	1200 $\pm$ 35	108 $\pm$ 2	0.53 $\pm$ 0.01	0.1712 $\pm$ 0.025	48.9
PES	1765 $\pm$ 50	1127 $\pm$ 35	83 $\pm$ 2	0.58 $\pm$ 0.01	0.1246 $\pm$ 0.013	267

\*: Average value in the range of 10 to 80 $^\circ\text{C}$ .

**Table 2.** Key parameters of the membrane module\*

Module type	PTFE-1	PTFE-2	PTFE-3	PES-1	PES-2	PES-3
N	3	6	9	4	8	12
$\varphi$ ( $\text{m}^2\text{m}^{-3}$ )	120.31	240.62	360.93	125.6	251.19	376.79
$\Phi$ (%)	5.88	11.76	17.64	5.54	11.08	16.61

\*: Outer diameters of membrane module, 17 mm; ID, inner diameters of membrane module, 15 mm; L, length of membrane module, 80 mm; N, number of the membrane in the module;  $\varphi$ , package density;  $\Phi$ , package fraction.

### 3.3 Solubility and metastable zone width (MSZW) measurement.

Thiourea was dissolved by stirring in water at the respective temperature over 12 h. The solutions were filtrated to remove the dissolved solids. The concentration of the solution was measured by an Abbe refractometer (Shanghai Precision Instrument Co., Ltd., China, 2WAJ) through a concentration-refractive index standard curve to determine the solubility. Measurement error is  $\pm 0.00002$  nD. The classic MSZW measurement method was introduced<sup>46</sup>.

All measurements were implemented in a 100 mL double-jacketed crystallizer. Easymax (Mettler Toledo Ltd.,

US, 102 HFCal) was used for temperature control and the stirring speed control. Laser transmitting and receiving devices (Thorlabs GmbH, PM100USB) were applied to determine the MSZW in the experiment based on the detective shape decrease in the laser light transmission intensity.

The solubility data of thiourea in water were measured by author and fitted via Apelblat simplified empirical equation<sup>2,6,47</sup> with a good agreement ( $R^2=0.99998$ ),

$$\ln x = 115.39 - \frac{8872.01398796}{(T+273)} - 14.54862211 \ln(T + 273) \quad (23)$$

where  $x$  is solubility of thiourea in water, g/100g water;  $T$  is temperature, °C.

The MSZW ( $\Delta T_{\max}$ ) was determined by the following equation:

$$\Delta T_{\max} = T_{\text{eq}} T \quad (24)$$

where  $T_{\text{eq}}$  is the equilibrium temperature of the thiourea aqueous solution at a certain concentration and  $T$  denote the detected initial nucleation temperature. As reported by Sangwal<sup>48</sup>, the theoretical model of the metastable zone width can be expressed as,

$$\ln \Delta T_{\max} = K + \frac{1}{m} \ln \nu - \frac{n}{m} \ln N_r \quad (25)$$

where  $\nu$  is cooling rate and  $N_r$  is stirring speed;  $K$ ,  $m$ ,  $n$  are experimental data regression parameters. A single-factor experiment was carried out to investigate the effect of operational conditions on MSZW, including cooling rate and stirring speed; the cooling rate ranged from 0.1 to 1 °C min<sup>-1</sup>; the stirring speed ranged from 100 to 500 rpm.

### 3.4 Nucleation induction period and surface tension measurement.

Apparatus in section 3.3 was also used to measure the nucleation induction period.  $t_{\text{ind}}$  in which the presence of the membrane and the absence of the membrane were tested at different stirring speeds. Induction period at different supersaturations based on different initial concentrations was measured based on the same initial concentration to determine the crystallization solution's surface tension. Different saturated thiourea solutions were placed in a water bath and rapidly cooled. Nucleation induction period was recorded and fitted to calculate the relevant surface tension with the classic method<sup>49</sup>.

### 3.5 MACC experiment.

Experimental setup of MACC is shown in Figure 3. The concentration of thiourea aqueous solution was 23.5 wt% (saturated at 39 degC). Crystallizer size ranged from 100 mL to 10 L (for the terminal comparison with conventional cooling crystallization, 10 L crystallizer was utilized). The thiourea aqueous solution was circulated into the membrane module through the shell side at a certain flow rate (range 200 to 400 mL min<sup>-1</sup>) by a fluid pump. The saturated thiourea solution was pumped into the membrane module when it decreased to the nucleation temperature. After the stable circulation reached, coolant was circulated through the tube side of the membrane module by a fluid pump. When sufficient number of crystal nucleus were appeared in the membrane module and recycled with the solution to the crystallizer, shut off the coolant and the solution transferred into a membrane module. Go on the cooling procedure in the crystallizer via following the cooling curve until the required yield reached. The high-speed microscopic camera was introduced as the online image monitoring unit to observe the nucleus particle motion on the membrane surface; PVM (Mettler Toledo Ltd, V19) was used for detecting crystal growth images and size distribution in the crystallizer. Then, the crystals product was filtrate and dried for further analysis.

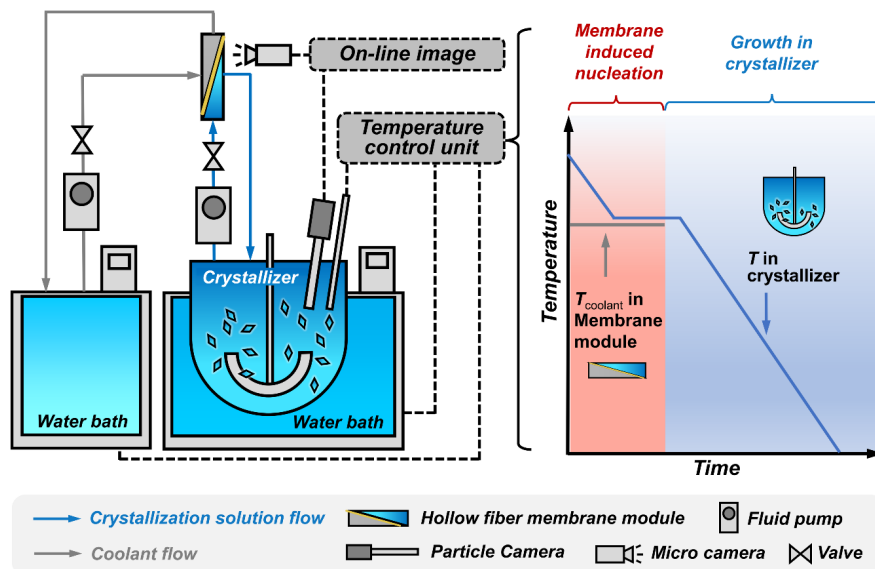


**Figure 3.** Experimental setup of MACC (left), the classic temperature route for membrane induced nucleation and growth in crystallizer (right).

Benefited from the high-speed microscopic camera, it can easily validate the theory proposed in section 2.2 and Figure 1b. Under the experimental condition, the crystals grew to certain size on the membrane surface. Then the crystal beyond a critical size automatically slipped from the membrane surface (shown in Figure 4). This phenomenon vividly represented the induced nucleation and auto-seeding process during MACC.

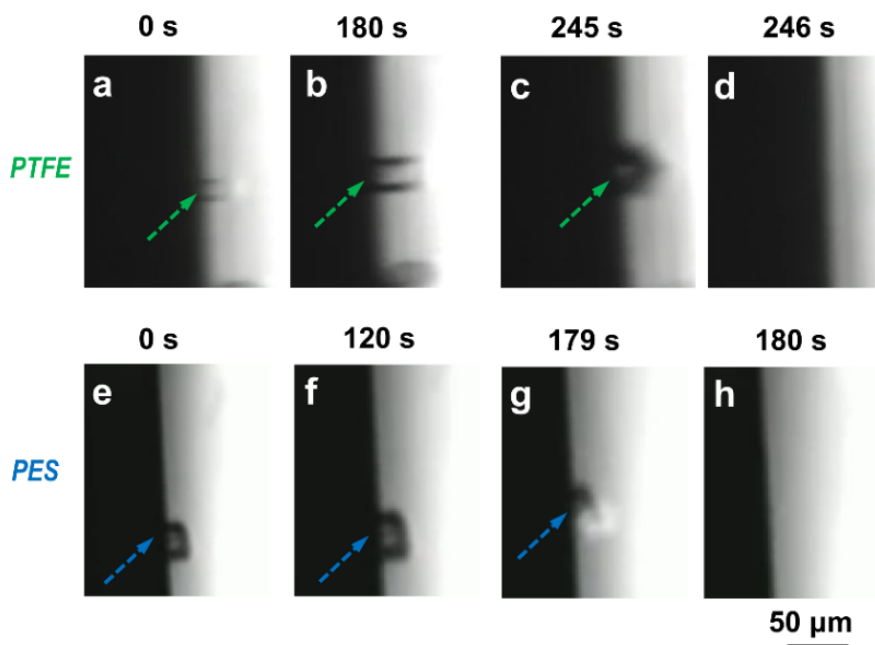


**Figure 4.** On-line observation of induced nucleation, crystal growth and self-detachment on the membrane surface.

### 3.6 Conventional cooling crystallization experiment.

Conventional cooling crystallization experiment (seeding and no seeding) was carried out as the comparison test. The initial concentration, volume of the crystallization solution, the cooling curve and operation conditions were all the same as in MACC process. The seeding temperature had been optimized and was also same with MACC. The seed amount was 1.5 wt% and 0.5 wt% of the yielding products, which were also optimized one. As a comparison, the crystals produced during the conventional experiment were also tested via the same method.

### 3.7 Solution penetration test.

The membrane module was the core equipment of the process. The experimental instrument was arranged similar to the experimental equipment used in MACC. The initial weight of the solution was recorded with a precision electronic balance (Baoding Signal fluid Technology Co.), and the heat exchange with the coolant is to be carried out. The weight of the solution was measured every minute. In the solution penetration test, it was found that the permeation of the two kinds of membranes were both very small, which the mass transfer process was ignorable. This result indicated the hypothesis that MACC possess only heat transfer process was true.

### 3.8 Characterization of crystal product

The shape and morphology images of the crystals in the slurry were obtained by optical microscope (Motic (Xiamen) Electric Group Co., Ltd., Motic SMZ-168), and then the crystal size distribution (CSD) was analyzed by Nano Measurer software. The results of each experiment were repeated more than three times and the average value was reported. Purity of the thiourea crystal is measured by the analytical laboratory of the Shandong Jingbo Co., Ltd. In alkaline condition, thiourea and iodine have quantitative reaction, while excess iodine solution was titrated with standard sodium thiosulfate, to obtain the content of thiourea.

## 4. Result and discussion

### 4.1 Thermal conductivity and interfacial property of PTFE and PES membrane.

PTFE and PES both have good mechanical stability and outstanding chemical resistance<sup>50-52</sup>. In addition, they both exhibit excellent reliability for rapid temperature floatation and for long-term usage as reported<sup>53</sup>. The measured thermal conductivity of PTFE and PES hollow fiber membranes are shown in Figure 5a. PTFE membrane possesses higher thermal conductivity ( $0.1712 \pm 0.025$  W/m·K, average value in the measured temperature range) than that of PES membrane ( $0.1246 \pm 0.013$  W/m·K). And the thermal conductivity of PTFE membrane increases from 0.1464 W/(m·K) to 0.1959 W/(m·K) when the temperature increases from 10 to 80 ; while, the thermal conductivity of PES membrane is relatively stable when the temperature increases. Generally, the thermal conductivity of the membrane is influenced by the nature of the membrane material (solid phase) and the pores distributed of in the membrane (gas phase). The large void structure in the membrane will be a convective heat transfer heat transfer and a radiation heat transfer mode<sup>54,55</sup>. The XRD patterns of the two membranes in Figure 5b indicates that the PTFE membrane possesses a semi-crystalline structure, whose thermal conductivity changes greatly with temperature<sup>56-58</sup>. While, PES membrane has an amorphous polymer, which the glass transition temperature is as high as 230 degC<sup>51</sup>. Below this temperature, the temperature has no significant impact on PES membrane's thermal conductivity. In the temperature operation range of 5 to 40 degC during MACC, the two hollow fiber membranes both have a stable thermal conductivity, which is important for the nucleation control at a wide temperature operation window.

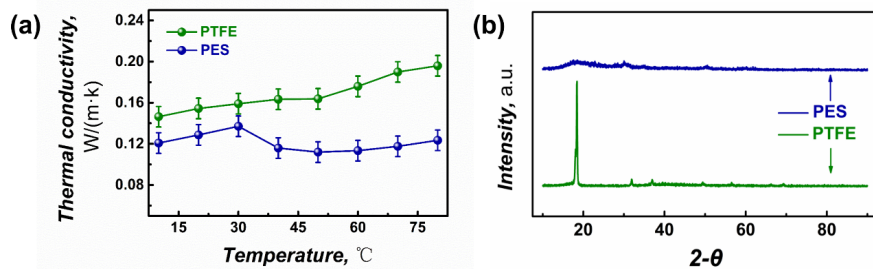


**Figure 5.** (a) Measured thermal conductivity and (b) XRD of PTFE and PES membrane.

In Figure 6, the roughness of the PES hollow fiber membrane is higher than that of the PTFE hollow fiber membrane. The membrane surface with high roughness and possible cavity will be easier to generate the heterogeneous nucleation on the membrane surface. While, the increasing surface roughness may restrain the auto-detachment motion of nucleation from the membrane surface. This complex impact on the membrane performance should be validated in the MACC operation<sup>59</sup>.

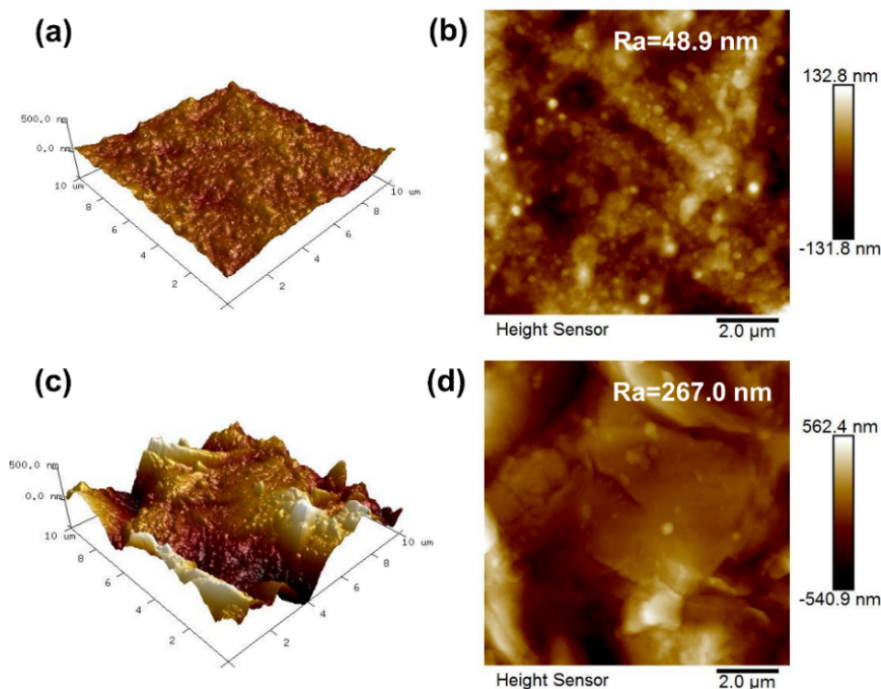


**Figure 6.** AFM (2D and 3D) images of the surface roughness of the PTFE membrane (a, b) and PES membrane (c, d).

The solution hydrophilicity is another property impacting the interfacial nucleation. As shown in Figure 7, PTFE and PES membrane surface had diverse surface contract properties with the thiourea aqueous solution. The contact angle of the PTFE hollow fiber membrane is around 108°, and the contact angle of the PES hollow fiber membrane is around 83°. The increasing concentration of thiourea (from 3 wt% to 12 wt%) had almost no influence on the contact angle, which ensure a stable nucleation control performance under wide feed solution concentration.

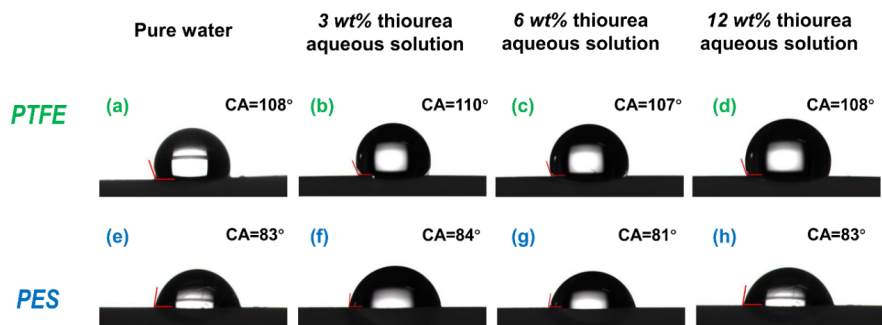


**Figure 7.** Contact angles of pure water and different thiourea aqueous solution on PTFE and PES hollow fiber membrane.

#### 4.2 MSZW in membrane-free operation.

The measured MSZW data of thiourea aqueous solution in membrane-free cooling crystallization under different cooling rate and stirring rate were listed in Table S1 as supporting materials. The measured MSZW data were calibrated using the least-squares method, which is,

$$\Delta T_{\max} = 40.9 \times \nu^{0.2625} N_r^{-0.4757}, R^2=0.964 \quad (26)$$

Comparison of experimental MSZW data and fitted ones also provided as supporting materials in Figure S1. According to the classical nucleation theory, high stirring intensity will accelerate the probability of particle collision to generate nucleation. It can also be seen that the MSZW tend to increase with the increase of the cooling rate due to the existence of the induction period. MSZW results provide the operation up limit for both membrane-free operation and membrane involved operation. MSZW under the membrane involved operation will be definitely lower than that of the membrane-free crystallization due to the inducing nucleation function of membrane. In this work, the rotating speed was set at 200 rpm to avoid the sever crystal breakage and secondary nucleation.

#### 4.3 Induction period and surface tension in MACC operation.

Based on the classic nucleation theory, the surface tension was determined by the induction period under different supersaturations<sup>36,60,61</sup>. In the low supersaturation zone, heterogeneous nucleation was dominant, and in the high supersaturation zone, homogeneous nucleation played the controlling role. The measured nucleation induction period with different membrane package density is as follows in the Figure 8.

Comparing the nucleation induction period with membrane module involved, it can be seen that the lower coolant temperature can provide the greater supercooling degree and correspondingly shorten the nucleation induction period under the tested temperature range. With increasing membrane module package density, the nucleation induction period almost inversely shortened (when PTFE membrane module package density increased from 120 m<sup>2</sup>/m<sup>3</sup> to 240.6 m<sup>2</sup>/m<sup>3</sup> then to 361.0 m<sup>2</sup>/m<sup>3</sup>, corresponding  $t_{\text{ind}}$  at 8 declined from 240s to 160s then to 80s). This result indicated that the nucleation induction period when the membrane module involved was highly impacted by the heat transfer property of the membrane module, which would also inevitably influence the membrane interface supercooling degree.

In addition, owing to roughness, hydrophobicity, and the thickness of membrane determines heterogeneous nuclear energy barrier of PES was smaller than that of PTFE, the induction time was also shorten when PES membrane module was introduced; The nucleation induction period with the same PTFE and PES membrane area were listed in Table 3. At the same terminal temperature, plotting  $\ln t_{\text{ind}}$  versus  $(\ln s)^{-2}$  yields two straight lines with different slopes, which represented the homogeneous nucleation and heterogeneous nucleation, respectively, which can be obtained by linear fitting (show in Figure S2 and S3 as supporting materials).

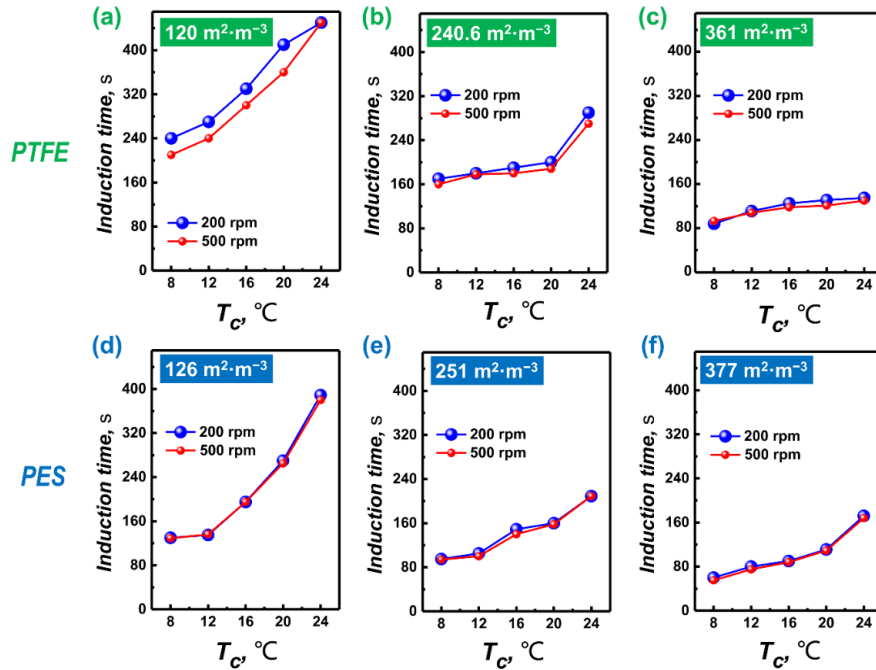


**Figure 8.** The nucleation induction period of thiourea in PTFE and PES membrane module with different package density. (membrane module type: (a) PTFE-1, (b) PTFE-2, (c) PTFE-3; (d) PES-1, (e) PES-2, (f) PES-3; number in the figure: package density of corresponding membrane module)

**Table 3.** The nucleation induction period within PTFE and PES membrane module (membrane package densities are  $361 \text{ m}^2 \cdot \text{m}^3$  and  $377 \text{ m}^2 \cdot \text{m}^3$ , respectively).

PTFE	PTFE	PES	PES
Relative supersaturation degree	induction period, s	Relative supersaturation degree	induction period, s
1.142	225	1.142	150
1.190	155	1.190	120
1.244	120	1.244	110
1.298	100	1.298	80
1.352	75	1.352	75
1.413	55	1.413	70

For the nucleation induction period with PTFE membrane, under high supersaturation,

$$\ln t_{\text{ind}} = 0.0933 (\ln s)^{-2} + 3.2500, R = 0.9859 \quad (27)$$

Under low supersaturation,

$$\ln t_{\text{ind}} = 0.0188 (\ln s)^{-2} + 4.3727, R = 0.9856 \quad (28)$$

According to the classical nucleation theory<sup>49</sup>, the intersection of these two lines should be the demarcation point of homogeneous nucleation and heterogeneous nucleation. The interfacial tension of thiourea at the corresponding temperature can be obtained from the heterogeneous nucleation slope and homogeneous nucleation slope. Thus, the solid-liquid interface tension of thiourea in the solution with PTFE membrane involved can be obtained,  $\gamma = 3.391 \text{ mJ/m}^2$ .

Similarly, for the nucleation induction period with PES membrane, under high supersaturation:

$$\ln t_{\text{ind}} = 0.0464 (\ln s)^{-2} + 3.7544, R = 0.9688 \quad (29)$$

Under low supersaturation:

$$\ln t_{\text{ind}} = 0.0077 (\ln s)^{-2} + 4.5629, R = 0.9647 \quad (30)$$

The solid-liquid interface tension of thiourea in the solution with PTFE membrane can be obtained,  $\gamma = 2.221 \text{ mJ/m}^2$ .

Surface tension required for heterogeneous nucleation on the PTFE hollow fiber membrane is  $3.391 \text{ mJ/m}^2$ , while PES hollow fiber membrane is  $2.221 \text{ mJ/m}^2$ . This is also consistent with the contact angles analyzed results in Figure 7, PES membrane possesses a higher affinity to the crystallization solution. Therefore, according to Eq. (2) to (6), heterogeneous nucleation barrier of PES hollow fiber membranes will be lower than that of PTFE membrane, which means PES MACC will possess higher nucleation rate  $B_p$  under the same supersaturation degree. The pre-exponential factor can be obtained from the Eq. (10). With the different contact angles and surface tension, the ratio of the heterogeneous nucleation rate between two kinds of membranes  $B_{p\text{-PES}}/B_{p\text{-PTFE}}$  is around 3.60.

While, the number of nuclei can be calculated from the total mass of the crystal product, the mass distribution of crystals. And with the known duration using membrane module to generate nuclei, we can evaluate the nucleation rate, semiquantitatively. The experimental data showed that the nucleation rate of the PES membrane was  $14.3 \text{ \#/mm}^3 \cdot \text{s}$ , the one of the PTFE membrane was  $4.0 \text{ \#/mm}^3 \cdot \text{s}$ , and the ratio is around 3.57, which was accompanied with the former theoretical research results of nucleation kinetics.

#### 4.4 MACC and the conventional cooling crystallization (CC)

With the known thermal and interfacial property of PTFE and PES membrane, MSZW for nucleation operation region, and nucleation kinetic relevant parameters (Induction period and surface tension) with membrane involved, we can furtherly investigate MACC with the other conventional CC.

Six different cooling crystallizations modes were discussed, MACC with PTFE hollow fiber membranes and PES hollow fiber membranes, common CC without membranes (average cooling rate is  $0.1 \text{ }^\circ\text{C/min}$ ), rapid CC (average cooling rate is  $0.5 \text{ }^\circ\text{C/min}$ ), CC with 0.5 wt% seed and 1.5 wt% seed addition. Except the rapid CC operation, the other operations have the same pre-setting cooling curve after the nucleation period, the terminal cooling temperature is also the same to ensure the same yield.

For the different nucleation inducing mechanism of the investigated tests, the solution temperature fluctuation in the crystallizer during nucleation period is an important evidence of the relevant controlling performance. The detective temperature in the crystallizer were listed in Figure 9. It can be seen from the figure that the solution temperature fluctuation peak of the PES MACC reached its peak at an early stage (around 0.20 at 100 s), which represented the latent heat mainly released by nucleation. This value was slightly higher than that of the PTFE MACC (0.08 ) with the similar membrane area. In addition, the peak of PES MACC appeared earlier than that of PTFE MACC, which also indicated that PES membrane is easier for induced heterogeneous nucleation. In fact, a moderate, controllable nucleation is longing for all the CC operation, and the smaller solution temperature fluctuation peak induced by nucleation will benefit the following nucleation and growth procedure. Herein, PTFE MACC possessed a better performance than that of FES MACC.

As for artificial seeding CC, with optimized crystal seed amount and seed timing, it is possible to maintain the solution temperature fluctuation under a favorable range (the peak for 1.5 wt% seed CC is 0.02 and the peak for 0.5 wt% seed CC is 0.21 , shown in Figure 9). While, the temperature fluctuation peak appeared much more later than that of MACC operation (around 800 to 900 s after seeding, which is one order of magnitude longer than MACC). This prolonged gap between the artificial seeding timing and bust nucleation heat release may stand for the persistent secondary nucleation. Because the artificial seeding introduced the exceeding amount of heterogeneous nucleation interface all at once without well dispersion, thus, in the crystallizer, the added seeds disperse with the stirring and will cause the unwanted, exceeding nucleation.

As an advantage of the MACC, by adjusting the temperature and flow rate in tube side and shell side of the membrane module, it is convenient to control the nucleation rate and auto-seeding amount that transferred into the crystallizer. Additionally, this membrane induced crystal seeds had uniform size distribution and were predispersed evenly by the crystallization solution.

As for spontaneous CC at different cooling rate, they both suffering the explosive nucleation at a later time, and the temperature fluctuation in the crystallizer increased significantly. With the increased cooling rate, this explosive nucleation was also accelerated (from 0.70 to 1.50, correspondingly).

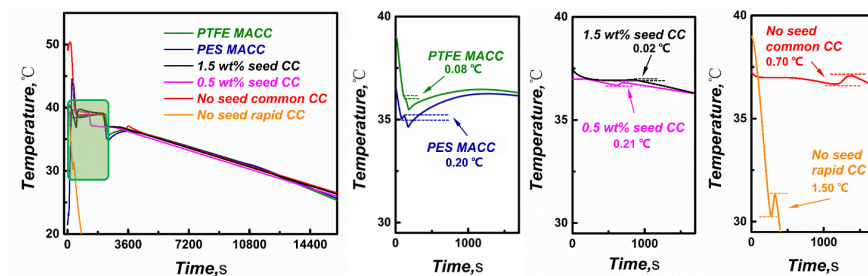


**Figure 9.** Comparison of solution temperature fluctuation in the crystallizer during nucleation period (PTFE MACC, PES MACC, seed CC with different seed amount and common CC with different cooling rate were listed).

CSD analysis results confirmed the advantages of MACC on the nucleation control and crystal growth (shown in Figure 10). At the initial period (Figure 10a), MACC and seed CC had the similar CSD, which illustrated the auto-seeding function of MACC. As expected, CC without seed had the widest CSD due to the uncontrollable spontaneous nucleation. While, with the nucleation occurred and crystal growth launched the competition under diverse supercooling degree, the different seeding mechanism began to present significantly different impact on the subsequent crystallization procedure. For the artificial seeding CC, the drawbacks of exceeding heterogeneous seeds interface introduced into the solution system abruptly became manifest. The exceeding secondary nucleation induced by the solid seed leading to the wider and wider CSD in the solution system (Figure 10b), which is an inherent problem that nucleation and growth competition in the same crystallization devices. While, for PTFE and PES MACC, illustrated in Figure 1, the stable nucleation and seed generation were realized in the membrane module, the feed flow suspended with uniform seeds transferred from membrane module to crystallizer effectively isolated the primary nucleation and crystal growth from space-time aspect. This new nucleation induced and seeding mechanism essentially decouple the nucleation and crystal growth, which then provided a feasible approach for controlling crystallization with high space-time accuracy. This new mechanism of MACC at the nucleation period had a profound and lasting effect on the CSD of terminal products (Figure 10c).

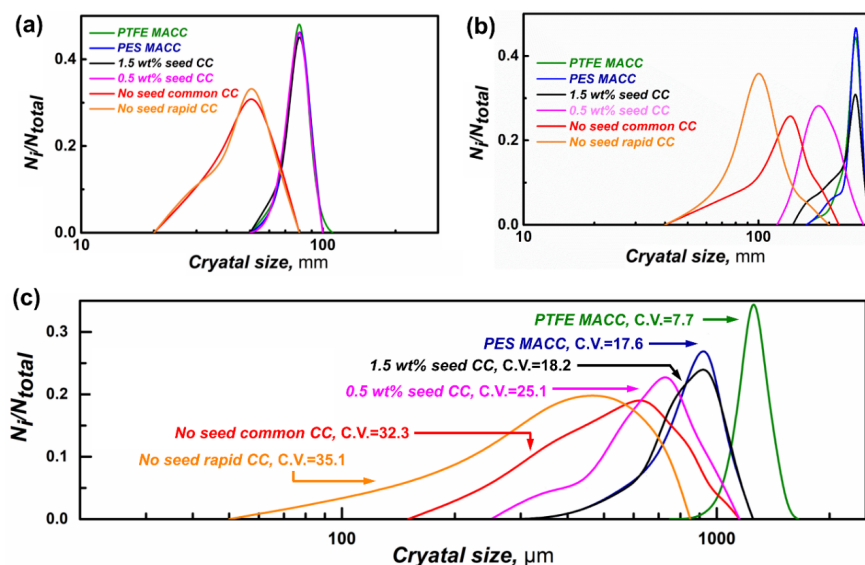


**Figure 10.** Comparison of crystal size distribution under different MACC and conventional cooling crystallization at different crystallization period. (a) 5 min after the initial nucleation (or seeding); (b) 10 min after the initial nucleation (or seeding); (c) terminal products.

Furtherly, on line detective images revealed more detailed information on the diverse crystallization process occurred in the crystallizer (Figure 11). At 5 min after initial nucleation (or seeding), uniform crystals can be detected in MACC operation, which validated the effective auto-seeding function and controllable secondary nucleation in the crystallizer. While, for common CC, only limited number of tiny nucleus can be observed. At 10 min after initial nucleation (or seeding), obvious crystal growth with uniform growth rate can be detected in MACC operation compared to common CC (with seed and without seed). The spontaneous nucleation caused the crystallizer in conventional CC filled with the tiny crystals, and the two kinds of seed CC showed different degrees of secondary nucleation.

The terminal crystal product manufactured by MACC had a regular shape, smooth surface as desirable crystal habit, big particle size without defects. However, there were too many defects on the crystal surface and agglomeration among the terminal product of CC without seeding, and the purity was only 99.0 wt% or less (2<sup>nd</sup> pure grade for industrial application). It can be seen that the terminal products manufactured via PTFE MACC and PES MACC both had significantly superior crystal purity (>99.5 wt%, exceeding 1<sup>st</sup> pure grade for industrial application) and desire morphology compared to all the conventional cooling crystallization (with seed and no seed). PTFE MACC has the most concentrated crystal size distribution (CV=7.7, mean size>1.35 mm) and the best crystal morphology.

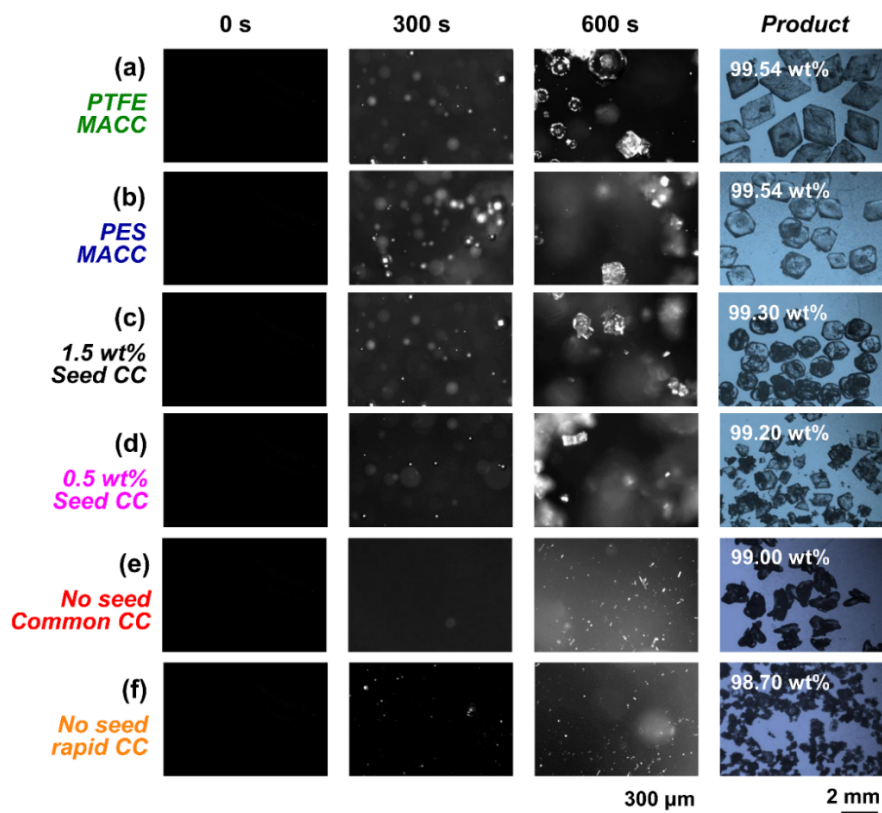


**Figure 11.** On line images of crystal nucleation, growth procedure in 10 L crystallizer and the terminal crystal products of different MACC and conventional cooling crystallization (with seed and no seed).

It was notable that all the MACC experiments were scaled up from 100 mL crystallizer to 2 L crystallizer then to 10 L crystallizer and had been repeated for more than ten times parallelly to indicate the stable nucleation and auto-seeding performance of the membrane module. In addition, the PTFE and PES hollow fiber membrane module utilized for MACC test had both be reused for more than one hundred times with stable performance, which is benefited by the excellent mechanical stability and chemical resistance of the chosen polymeric materials.

## 5. Conclusions

A novel MACC technology was developed and comprehensively investigated to realize the automatic and accurate control of thiourea cooling crystallization, which governed by the heterogeneous nucleation and automatic screening on the PTFE and PES hollow fiber membrane interfaces. With effective interfacial heat transfer, the mechanism of membrane interface induced nucleation and process control was fully validated via the nucleation research and on-line monitoring. The overwhelming performance of MAAC reflects as dominating the accurate nucleation kinetic and hindering the secondary nucleation effectively, which resulting in the high purity, desire product morphology and very narrow CSD compared to that of conventional cooling crystallization (both artificial seeding and spontaneous nucleation operations were compared). Space-time process decoupling via surface nucleation in the membrane module and crystal growth in crystallizer, which is the core feature of the developed MACC, is a novel path for accurate crystallization control and process intensification.

## Acknowledgement

We acknowledge the financial contribution from National Natural Science Foundation of China (Grant No.

21676043, 21527812, U1663223, 21978037), MOST innovation team in key area (No. 2016RA4053) and Fundamental Research Funds for the Central Universities (DUT19TD33).

### Literature Cited

1. Sun XX, Sun YZ, Yu JG. Cooling crystallization of aluminum sulfate in pure water. *Journal of Crystal Growth*. Jun 2015;419:94-101.
2. Schall JM, Mandur JS, Braatz RD, Myerson AS. Nucleation and Growth Kinetics for Combined Cooling and Antisolvent Crystallization in a Mixed-Suspension, Mixed-Product Removal System: Estimating Solvent Dependency. *Cryst. Growth Des.* Mar 2018;18(3):1560-1570.
3. Jensen KF. Flow chemistry-Microreaction technology comes of age. *Aiche J.*2017;63(3):858-869.
4. Yang GY, Kubota N, Sha ZL, Louhi-Kultanen M, Wang JF. Crystal shape control by manipulating supersaturation in batch cooling crystallization. *Cryst. Growth Des.* Dec 2006;6(12):2799-2803.
5. Kim KJ, Doherty MF. Crystallization of Selective Polymorph Using Relationship Between Supersaturation and Solubility. *Aiche Journal*. Apr 2015;61(4):1372-1379.
6. Li P, He G, Lu D, Xu X, Chen S, Jiang X. Crystal Size Distribution and Aspect Ratio Control for Rodlike Urea Crystal via Two-Dimensional Growth Evaluation. *Industrial & Engineering Chemistry Research*.2017;56(9):2573-2581.
7. Lenka M, Sarkar D. Improving crystal size distribution by internal seeding combined cooling/antisolvent crystallization with a cooling/heating cycle. *Journal of Crystal Growth*. Mar 2018;486:130-136.
8. Narducci O, Jones AG. Seeding in Situ the Cooling Crystallization of Adipic Acid using Ultrasound. *Cryst. Growth Des.* Apr 2012;12(4):1727-1735.
9. Paulson JA, Mesbah A, Zhu XX, Molaro MC, Braatz RD. Control of self-assembly in micro- and nano-scale systems. *J. Process Control*. Mar 2015;27:38-49.
10. Kleetz T, Braak F, Wehenkel N, Schembecker G, Wohlgemuth K. Design of Median Crystal Diameter Using Gassing Crystallization and Different Process Concepts. *Cryst. Growth Des.* Mar 2016;16(3):1320-1328.
11. Agrawal S, Guest JS, Cusick RD. Elucidating the impacts of initial supersaturation and seed crystal loading on struvite precipitation kinetics, fines production, and crystal growth. *Water Research*. Apr 1 2018;132:252-259.
12. Zuo J, Chung T-S. In-situ cross-linked PVDF membranes with enhanced mechanical durability for vacuum membrane distillation. *Aiche Journal*. Nov 2016;62(11):4013-4022.
13. Adrjanowicz K, Koperwas K, Paluch M. Isobaric Cooling or Isothermal Compression? Unveiling the Effect of Path Dependence on Crystallization. *Cryst. Growth Des.*Jun 2017;17(6):2950-2954.
14. Lu DP, Li P, Xiao W, He GH, Jiang XB. Simultaneous recovery and crystallization control of saline organic wastewater by membrane distillation crystallization. *Aiche Journal*. Jun 2017;63(6):2187-2197.
15. Alpatova A, Alsaadi AS, Alharthi M, Lee JG, Ghaffour N. Co-axial hollow fiber module for air gap membrane distillation. *Journal of Membrane Science*. May 15 2019;578:172-182.
16. Cheng C, Shao Z, Vollrath F. Silk Fibroin-Regulated Crystallization of Calcium Carbonate. *Adv Funct Mater*. 2008;18(15):2172-2179.
17. Zimmermann NER, Vorselaars B, Quigley D, Peters B. Nucleation of NaCl from Aqueous Solution: Critical Sizes, Ion-Attachment Kinetics, and Rates. *Journal of the American Chemical Society*. Oct 21 2015;137(41):13352-13361.

18. Jiang X, Lu D, Xiao W, Ruan X, Fang J, He G. Membrane assisted cooling crystallization: Process model, nucleation, metastable zone, and crystal size distribution. *AIChE Journal*. 2016;62(3):829-841.
19. Jiang X, Lu D, Xiao W, et al. Interface-based crystal particle autoselection via membrane crystallization: From scaling to process control. *AIChE Journal*. 2019;65:723-733.
20. Song L, Li B, Zarkadas D, Christian S, Sirkar KK. Polymeric Hollow-Fiber Heat Exchangers for Thermal Desalination Processes. *Ind. Eng. Chem. Res.* Dec 1 2010;49(23):11961-11977.
21. Zarkadas DM, Sirkar KK. Solid hollow fiber cooling crystallization. *Ind. Eng. Chem. Res.* Oct 2004;43(22):7163-7180.
22. Iliuta I, Iliuta MC. Investigation of CO<sub>2</sub> removal by immobilized carbonic anhydrase enzyme in a hollow-fiber membrane bioreactor. *Aiche Journal*. Jul 2017;63(7):2996-3007.
23. Tuo L, Ruan X, Xiao W, Li X, He G, Jiang X. A novel hollow fiber membrane-assisted antisolvent crystallization for enhanced mass transfer process control. *AIChE Journal*. 2019;65:734-744.
24. Wang Q, Zeng M, Ma T, Du X, Yang J. Recent development and application of several high-efficiency surface heat exchangers for energy conversion and utilization. *Applied Energy*. Dec 15 2014;135:748-777.
25. Krasny I, Astrouski I, Raudensky M. Polymeric hollow fiber heat exchanger as an automotive radiator. *Appl. Therm. Eng.* Sep 2016;108:798-803.
26. Ghaebi H, Namin AS, Rostamzadeh H. Exergoeconomic optimization of a novel cascade Kalina/Kalina cycle using geothermal heat source and LNG cold energy recovery. *Journal of Cleaner Production*. Jul 10 2018;189:279-296.
27. da Silva G, Dlugogorski BZ, Kennedy EM. Water-in-oil emulsion foaming by thiourea nitrosation: Reaction and mass transfer. *Aiche Journal*. Apr 2006;52(4):1558-1565.
28. Charalampopoulos VG, Kariuki BM, Harris KDM. Complexes of Thiourea with Alkali Metal Bromides and Iodides: Structural Properties, Mixed-Halide and Mixed-Metal Materials, and Halide Exchange Processes. *Cryst. Growth Des.* Feb 2017;17(2):786-793.
29. Wu D, Inventor; Anhui Jianyuan Medical Instr Equip Co, assignee. Silicone rubber material useful for preparation of medical products, contains silicone rubber, acrylic rubber, polyvinyl alcohol, paraffin, hydrogen peroxide, polyvinylpyrrolidone, thermoplastic polyurethane, preservative and thiourea. US patent CN107815120-A.
30. Ullah B, Zhou Y, Chen J, et al. New catalytic effect of thiourea on the oxidative cyanation of N-aryltetrahydroisoquinolines. *Tetrahedron Letters*. Jan 24 2019;60(4):348-351.
31. Habila T, Belghobsi M, Stiti M-Z, et al. Synthesis and vasodilator activity of 3,4-dihydropyrimidin-2(1H)-ones bearing urea, thiourea, and sulfonylurea moieties. *Canadian Journal of Chemistry*. Jan 2019;97(1):20-28.
32. Ding L, Liu F, Wu P, et al., Inventors; Univ Taiyuan Ind (Untl-C), assignee. High-purity copper cathode composite additive comprises plastic additive, thiourea, casein, chloride and rare earth salt, where gum additive contains bone glue, gelatin, guar gum, acacia gum, polyacrylamide hydrogel and guar gum. US patent CN105132946-A. CN105132946-A 09 Dec 2015 C25C-001/12 201634.
33. Diao P, Xue N, Inventors; Univ Beihang (Unba-C), assignee. Preparation of molybdenum disulfide/carbon black composite electrocatalytic material used for hydrogen evolution, involves reacting carbon black oxide with sodium molybdate dihydrate and thiourea, centrifuging, washing and drying. US patent CN105200450-A; CN105200450-B. CN105200450-A 30 Dec 2015 C25B-011/06 201642.
34. Yan SF, Xie C, Zhang X, et al. Influence of Crystal Growth Conditions on Formation of Macroscopic Inclusions inside Thiourea Crystals. *ChemistrySelect*. Feb 2018;3(8):2293-2297.

- 35.** Guo L, Yan Z, Feng C, Liang C, Peng Z, Inventors; Hebei Xinji Chem Ind Group Co Ltd, assignee. Thiourea continuous crystallization device, has cooler connected with crystallizer through circulating liquid inlet pipe, and outlet pipe connected with pipe outlet, where inlet pipe is connected with circulating liquid pipe inlet. US patent CN207137414-U.
- 36.** Kleetz T, Funke F, Sunderhaus A, Schembecker G, Wohlgemuth K. Influence of Gassing Crystallization Parameters on Induction Time and Crystal Size Distribution. *Cryst. Growth Des.* Dec 2016;16(12):6797-6803.
- 37.** Ahn J, Kim DH, Coquerel G, Kim WS. Chiral Symmetry Breaking and Deracemization of Sodium Chlorate in Turbulent Flow. *Cryst. Growth Des.* Jan 2018;18(1):297-306.
- 38.** Lakshtanov LZ, Belova DA, Okhrimenko DV, Stipp SLS. Role of Alginate in Calcite Recrystallization. *Cryst. Growth Des.* Jan 2015;15(1):419-427.
- 39.** Karthika S, Radhakrishnan TK, Kalaichelvi P. A Review of Classical and Nonclassical Nucleation Theories. *Cryst. Growth Des.* Nov 2016;16(11):6663-6681.
- 40.** Li Q, Rudolph V, Peukert W. London-van der Waals adhesiveness of rough particles. *Powder Technology.* Feb 3 2006;161(3):248-255.
- 41.** O'Neill ME. A SPHERE IN CONTACT WITH A PLANE WALL IN A SLOW LINEAR SHEAR FLOW. *Chemical Engineering Science.* 1968 1968;23(11):1293-&.
- 42.** Zhang M, Akbulut M. Adsorption, Desorption, and Removal of Polymeric Nanomedicine on and from Cellulose Surfaces: Effect of Size. *Langmuir.* Oct 18 2011;27(20):12550-12559.
- 43.** Jiang XB, Lu DP, Xiao W, et al. Interface-based crystal particle autoselection via membrane crystallization: From scaling to process control. *Aiche Journal.* Feb 2019;65(2):723-733.
- 44.** Gilbert PH, Saengow C, Giacomini AJ. Transport Phenomena in Eccentric Cylindrical Coordinates. *Aiche Journal.* Aug 2017;63(8):3563-3581.
- 45.** Karthik GM, Buwa VV. Effect of particle shape on fluid flow and heat transfer for methane steam reforming reactions in a packed bed. *Aiche Journal.* Jan 2017;63(1):366-377.
- 46.** Hou H, Wang JL, Chen LZ, Lan GC, Li J. Experimental determination of solubility and metastable zone width of 3,4-bis(3-nitrofurazan-4-yl)furoxan (DNTF) in (acetic acid plus water) systems from (298.15 K-338.15 K). *Fluid Phase Equilib.* Jan 2016;408:123-131.
- 47.** Kim H, Park K, Chang JW, Lee T, Kim SH, Yang DR. Solubility Measurement and Recrystallization Process Design for 1,1,2,2,9,9,10,10-Octafluoro 2.2 paracyclophane (AF4) Purification. *Cryst. Growth Des.* Mar 2019;19(3):1748-1755.
- 48.** Sangwal K, Mielniczek-Brzówska E, Barylska S. Solubility of ammonium oxalate in water-acetone mixtures and metastable zone width of their solutions. *Chemical Engineering Research & Design.* 92(3):491-499.
- 49.** Du GC, Sun ZH, Xian Y, Jing H, Chen HJ, Yin DF. The nucleation kinetics of ammonium metavanadate precipitated by ammonium chloride. *Journal of Crystal Growth.* May 2016;441:117-123.
- 50.** Liu B, Robertson GP, Kim D-S, Sun X, Jiang Z, Guiver MD. Enhanced thermo-oxidative stability of sulfophenylated poly(ether sulfone)s. *Polymer.* Jan 21 2010;51(2):403-413.
- 51.** Arzhakova OV, Dolgova AA, Rukhlya EG, Volynskii AL. Environmental crazing and properties of mesoporous and nanocomposite materials based on poly(tetrafluoroethylene) films. *Polymer.* Jan 2019;161:151-161.
- 52.** Khorshidi B, Hosseini SA, Ma GB, McGregor M, Sadrzadeh M. Novel nanocomposite polyethersulfone-antimony tin oxide membrane with enhanced thermal, electrical and antifouling properties. *Polymer.* Feb 2019;163:48-56.

53. Tuo L, Ruan X, Xiao W, Li X, He G, Jiang X. A novel hollow fiber membrane-assisted antisolvent crystallization for enhanced mass transfer process control. *Aiche Journal*. Feb 2019;65(2):734-744.
54. Pinto J, Notario B, Verdejo R, Dumon M, Costeux S, Rodriguez-Perez MA. Molecular confinement of solid and gaseous phases of self-standing bulk nanoporous polymers inducing enhanced and unexpected physical properties. *Polymer*. Mar 2017;113:27-33.
55. Schick C, Androsch R, Schmelzer JWP. Homogeneous crystal nucleation in polymers. *J. Phys.-Condes. Matter*. Nov 2017;29(45):35.
56. Irfan M, Idris A. Overview of PES biocompatible/hemodialysis membranes: PES-blood interactions and modification techniques. *Mater. Sci. Eng. C-Mater. Biol. Appl.* Nov 2015;56:574-592.
57. Babaahmadi M, Sabzi M, Mandavinia GR, Keramati M. Preparation of amorphous nanocomposites with quick heat triggered shape memory behavior. *Polymer*. Mar 10 2017;112:26-34.
58. Choi UH, Kwon YK, Lee M. Correlating morphology to thermal and electrical properties in imidazolium-poly(ethylene glycol) copolyesters. *Polymer*. Jun 2018;146:420-428.
59. Thamaraiselvan C, Carmiel Y, Eliad G, Sukenik CN, Semiat R, Dosoretz CG. Modification of a polypropylene feed spacer with metal oxide-thin film by chemical bath deposition for biofouling control in membrane filtration. *Journal of Membrane Science*. Mar 2019;573:511-519.
60. Kim KJ, Mersmann A. Estimation of metastable zone width in different nucleation processes. *Chemical Engineering Science*. Apr 2001;56(7):2315-2324.
61. Chen J, Mosquera-Giraldo LI, Ormes JD, Higgins JD, Taylor LS. Bile Salts as Crystallization Inhibitors of Supersaturated Solutions of Poorly Water-Soluble Compounds. *Cryst. Growth Des.* Jun 2015;15(6):2593-2597.

## Figure captions

**Figure 1.** Principle of MACC and comparison with classic cooling crystallizations. (a) Schematic diagram of the ideal MACC process; (b) Micro force field model of surface induced nucleation and self-seeding process (c) Comparison of the different force acting on the crystal with different size; (d) Heat transfer model of membrane module in MACC; (e) cooling crystallization with artificial seeding; (f) cooling crystallization with spontaneous nucleation.

**Figure 2.** SEM for the microstructure of PTFE membrane (a-f) and PES membrane (g-l).

**Figure 3.** Experimental setup of MACC (left), the temperature route for membrane induced nucleation and growth in crystallizer (right).

**Figure 4.** On-line observation of crystal growth and self-detachment on the membrane surface.

**Figure 5.** (a) Measured thermal conductivity and (b) XRD of PTFE and PES membrane.

**Figure 6.** AFM (2D and 3D) images of the surface roughness of the PTFE membrane (a, b) and PES membrane (c, d).

**Figure 7.** Contact angles of pure water and different thiourea aqueous solution on PTFE and PES hollow fiber membrane.

**Figure 8.** The nucleation induction period of thiourea in PTFE and PES membrane module with different package density. (membrane module type: (a) PTFE-1, (b) PTFE-2, (c) PTFE-3; (d) PES-1, (e) PES-2, (f) PES-3; number in the figure: package density of corresponding membrane module)

**Figure 9.** Comparison of solution temperature fluctuation in the crystallizer during nucleation period (PTFE MACC, PES MACC, seed CC with different seed amount and common CC with different cooling rate were listed).

**Figure 10.** Comparison of crystal size distribution under different MACC and conventional cooling crystallization at different crystallization period. (a) 5 min after the initial nucleation (or seeding); (b) 10 min after the initial nucleation (or seeding); (c) terminal products.

**Figure 11.** On line images of crystal nucleation, growth procedure in 10 L crystallizer and the terminal crystal products of different MACC and conventional cooling crystallization (with seed and no seed).